VNU Journal of Science: Mathematics - Physics
Journal homepage: https://js.vnu.edu.vn/MaP

Original Article

High-performance Magnetoimpedance Sensors in Micropatterned Multi-meander Line Designs

Ngo Thi Thanh[1], Nguyen Van Tuan[2], Dang Huy Hoang[1], Pham Minh Vuong[1], Hoang Si Hong[3], Do Duy Phu[4], Ho Anh Tam[1], Vu Nguyen Thuc[1], Do Thi Huong Giang[1,*]

[1]*VNU University of Engineering and Technology, 144 Xuan Thuy, Cau Giay, Hanoi, Vietnam*
[2]*Le Quy Don Technical University, 236 Hoang Quoc Viet, Bac Tu Liem, Hanoi, Vietnam*
[3]*School of Electrical and Electronic Engineering, Hanoi University of Science and Technology, 1 Dai Co Viet, Hai Ba Trung, Hanoi, Vietnam*
[4]*School of Electrical and Electronic Engineering, Hanoi University of Industrial, 298 Cau Dien, Bac Tu Liem, Hanoi, Vietnam*

Received 18th April 2025
Revised 27th May 2025; Accepted 16th June 2025

Abstract: In this work we present the design and fabrication of micro-scale magnetoimpedance (MI) sensors based on FeSiC soft magnetic ribbon, using laser engraving and chemical etching to create conventional meander (1M), meander structures in parallel (4Mpa) and perpendicular (4Mpe) configurations. Experimental characterization and finite element simulations revealed that assembling four meander elements enhances the MI effect by up to an order of magnitude compared to the 1M sensor. The 4Mpa configuration exhibits strong anisotropic MI response and lower frequency resonance of 1.5 GHz, while the 4Mpe structure offers a slightly lower MI ratio of 180% but with near-isotropic behavior. These differences arise from uniaxial versus multi-axial magnetic anisotropy, respectively, thanked to the numerical simulation. The results demonstrate that sensor performance can be tailored by selecting appropriate meander arrangements, enabling enhanced sensitivity and directional control for diverse applications in biomedical, industrial, and high-frequency sensing fields.

Keywords: Magnetoimpedance, Magnetic energy, Meander design, Magnetic anisotropy.

* Corresponding author.
E-mail address: giangdth@vnu.edu.vn

https//doi.org/10.25073/2588-1124/vnumap.5002

1. Introduction

Magnetic sensors have become indispensable across a broad spectrum of technological domains, including medical diagnostics, military systems, precision measurement, inspection, and integration within advanced industrial robotics [1, 2]. Among the various sensor technologies, magnetoimpedance (MI) sensors have emerged as particularly promising due to their exceptional attributes, i.e., high sensitivity, rapid response, and the potential for isotropic operation, which are positioning them as strong competitors to established magnetic sensor technologies such as Hall effect, anisotropic magnetoresistance, giant magnetoresistance, and fluxgate sensors [3-6].

The MI effect is defined as the substantial change in the complex impedance of a soft magnetic conductor when subjected to an external DC magnetic field while a high frequency alternating current is applied [7]. This phenomenon is fundamentally governed by the classical skin effect, whereby the penetration depth of the alternating current is inversely related to the material's conductivity, magnetic permeability, and the frequency of the current [8]. As a result, materials with high conductivity and permeability exhibit reduced skin depth, thereby amplifying the MI response and enabling high sensitivity to external magnetic fields [1, 6].

With the ongoing miniaturization of electronic devices and advancements in high-speed signal processing, there is a growing demand for compact, high-performance magnetic sensors. Thin films and soft magnetic strips are particularly attractive for integration with microelectronic systems due to their small size and compatibility with modern fabrication processes [1, 6]. However, miniaturization can exacerbate demagnetization effects, which may degrade magnetic properties and diminish the MI effect [9, 10]. To address these challenges and optimize sensor performance, it is essential to conduct in-depth investigations into the intrinsic factors influencing the MI effect, including shape anisotropy and the impact of demagnetizing fields.

The geometry and structural design of the sensing element are critical determinants of MI sensor performance, influencing not only the magnitude of the MI effect but also the sensitivity and resolution of the device. Variations in sensor architecture such as multilayer, straight-rod, or meander configurations can significantly modulate the MI response in soft magnetic materials [1, 6, 11, 12]. In addition to material selection and fabrication process optimization (e.g., annealing, doping), the deliberate engineering of sensor shape and structure represents a key strategy for enhancing MI sensor functionality [10, 13-15]. Among contemporary sensor architectures, the meander structure, characterized by a zigzag arrangement of thin conductive or resistive strips, has garnered significant attention. This design increases the effective conduction length within a compact footprint, thereby maximizing the interaction area with the external magnetic field and enhancing MI sensitivity without enlarging the sensor [1, 6, 11, 12]. Furthermore, meander patterns are well-suited for integration with microelectronic circuits and can be engineered to optimize sensor response for specific applications.

Leveraging the principles of bridge circuit design, which enables precise measurement of small resistance changes, this research focuses on the development of a sensor array comprising four meander elements connected in a resistor bridge configuration. This approach aims to maximize the sensor's active area and MI response, facilitating accurate and sensitive magnetic field detection for practical applications. The scope of this work encompasses a comprehensive analysis of the magnetic properties of the constituent materials, characterization of the MI effect, and systematic investigation of the roles of magnetic anisotropy and demagnetization fields in determining sensor performance. Additionally, the influence of coupling configurations, i.e., parallel versus perpendicular easy axis alignments, within the bridge structure on the MI effect will be elucidated through a combination of experimental measurements and finite element numerical simulations.

2. Methodology

In this work, the MI sensors were fabricated using a magnetically soft $Fe_{90.88}Si_{4.13}C_{4.99}$ (FeSiC) commercial ribbon with a nominal thickness of 20 μm, employing a combination of wet chemical etching

and laser engraving to achieve the defined structures. The fabrication procedure consists of three main stages, as outlined in Fig. 1a and based on parameters established in previous studies [16, 17]. Initially, the FeSiC ribbon was affixed to a substrate and coated with a thin protective paint layer serving as an etching mask. Laser engraving was then utilized to selectively pattern the masked ribbon, as depicted in Fig. 1, a1). Following this, the patterned sample underwent wet chemical etching in a solution composed of HNO_3:HCl:H_2O:H_2O_2 (Fig. 1, a2), where precise control of etching duration and reagent ratios ensured complete removal of unprotected regions while preserving the masked areas. The final step involved removing the masking layer with acetone, followed by ultrasonic cleaning in alcohol, rinsing with deionized water, and drying, resulting in a sensor with the desired microstructured geometry (Fig. 1, a3).

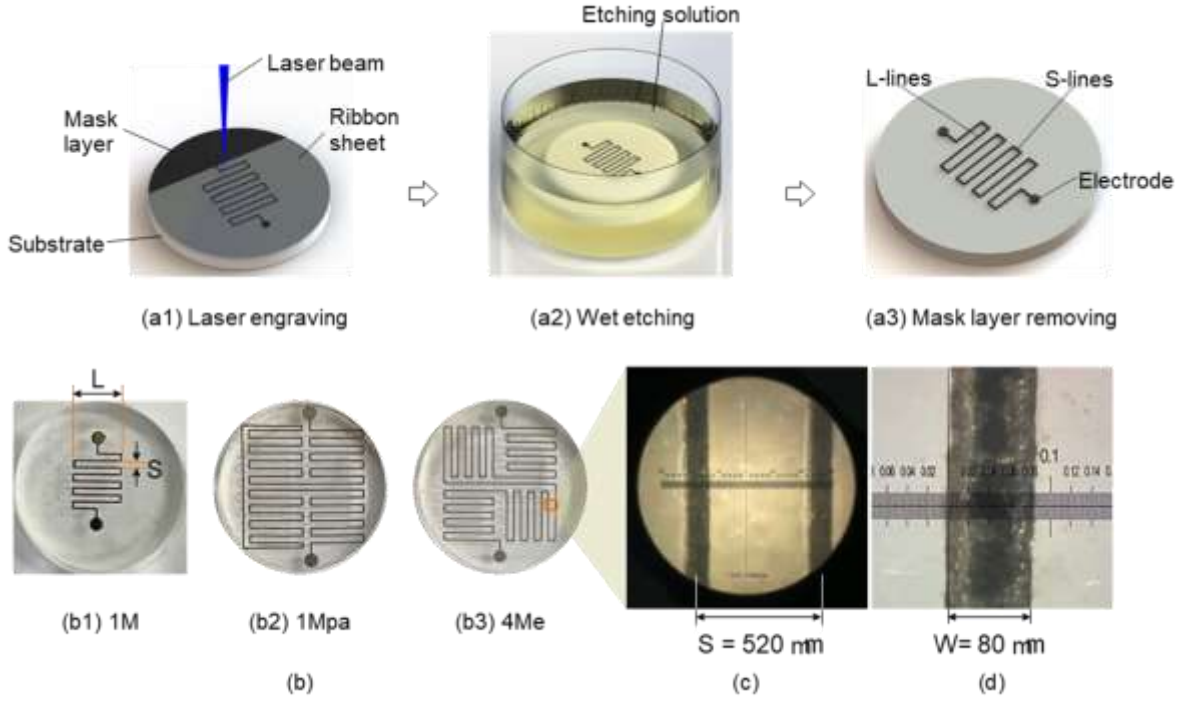

Figure 1. (a) Sample fabrication processes: layer mask spin coating and laser engraving (a1), wet etching (a2), mask layer removing; (b) pictures and optical microscope images of sample after fabrication.

Fig. 1b presents optical images of the three distinct sample architectures investigated in this work: a single meander line (denoted as 1M, Fig. 1, b1), and two foursegment meander arrays configured in parallel (4Mpa, Fig. 1 (b2)) and perpendicular (4Mpe, Fig. 1, b3) orientations. Within each meander structure, the design incorporates alternating long (L-lines, L = 3.6 mm) and short (S-lines, S = 520 µm) bars, as schematically depicted in Fig. 1, a3. High-resolution optical micrographs (Fig. 1d) confirm that the fabricated structures exhibit smooth surfaces and well-defined, straight boundaries, with a consistent line width of approximately W = 80 µm. The fabrication methodology combining laser engraving and wet chemical etching employed in this study was comprehensively investigated in our previous work [16, 17]. These investigations confirmed that the compositional and structural properties of the samples remain essentially unchanged following the fabrication processes. Notably, the fabricated samples retained their amorphous phase without any detectable crystallization. Furthermore, the reproducibility of the developed sensor set was systematically evaluated and verified, demonstrating consistent fabrication outcomes.

The magnetic properties of the fabricated MI sensor samples were systematically characterized using a vibrating sample magnetometer (VSM, Lakeshore 7400 series), with applying magnetic fields up to 0.5 T. Measurements were conducted at multiple φ-angle orientations between the applied field and the long axes (L-lines) of the structures to elucidate angular dependence of magnetic behavior. For MI characterization, the samples were electrically contacted at both ends and assessed using a Protek A333 network analyzer, spanning frequencies up to 3.2 GHz. MI measurements were performed under external magnetic fields up to 0.04 T and at various φ-angles to capture the anisotropic response. To complement the experimental investigation, finite element simulations were performed using Ansys Maxwell software to analyze the magnetic anisotropy and the magnetization response of both 1M and 4M meander structures, enabling a comprehensive understanding of the interplay between geometry, anisotropy, and MI performance.

3. Results and Discussions

3.1. Magnetic Characteristics

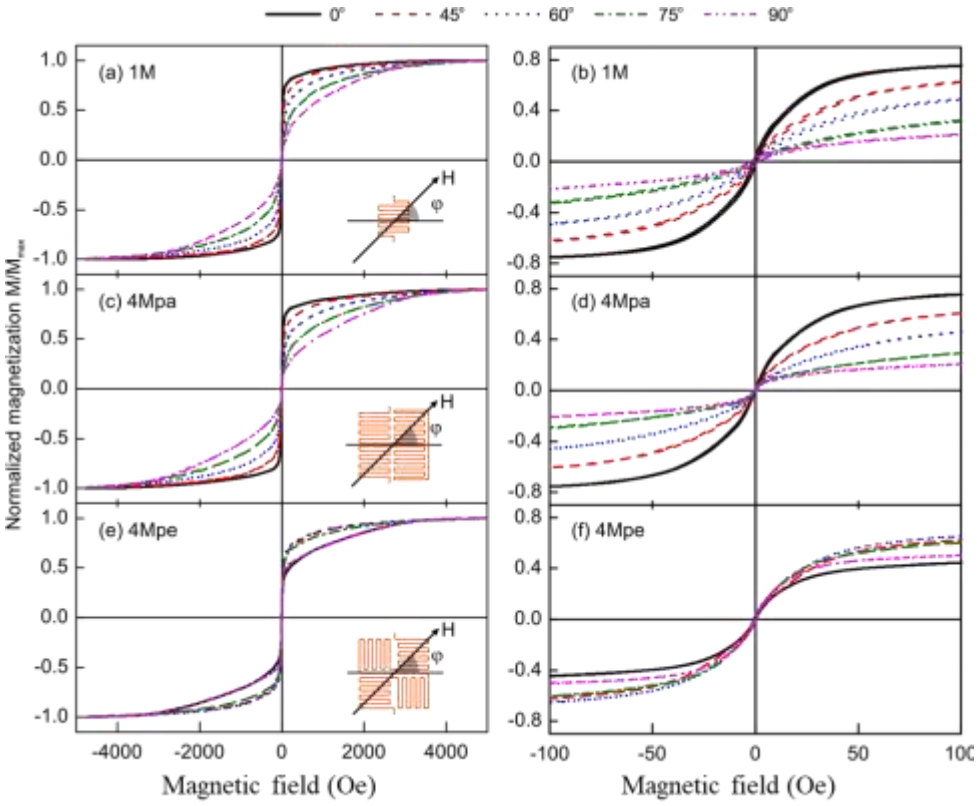

Figure 2. Normalize magnetization loop plotted in full (a) and small magnetic field range(b) for various samples with different configuration from single to 4 meander units in parallel and perpendicular alignment.

Fig. 2 presents the normalized magnetization (M/M_{max}) as a function of applied magnetic field over a wide range of ±5000 Oe (±0.5 T) and a focused range of ±100 Oe for samples with varying configurations, including 1M, 4Mpa, and 4Mpe. Characterizations were conducted at different angular orientations (φ) between the external magnetic field and the baseline of the structures (as defined in the insets in Fig. 2). At φ = 0°, all samples exhibit typical soft magnetic behavior characterized by rapid magnetization response

within low fields below 50 Oe. Beyond this region, magnetization increases more gradually, reaching saturation only at relatively high fields near 0.35 T. The low-field magnetization loops reveal minimal coercivity values below 0.5 Oe, consistent with the intrinsic properties of amorphous soft magnetic ribbon, indicating that the fabrication processes preserve the magnetic integrity of the FeSiC material. Angular dependence studies show that the magnetization curves of 1M, 4Mpa, and 4Mpe structures strongly depend on the measurement angle, with increasing φ resulting in a slower approach to saturation, reflecting anisotropic magnetic behavior. In contrast, the 4Mpe configuration exhibits markedly reduced angular dependence, suggesting a more isotropic magnetic response.

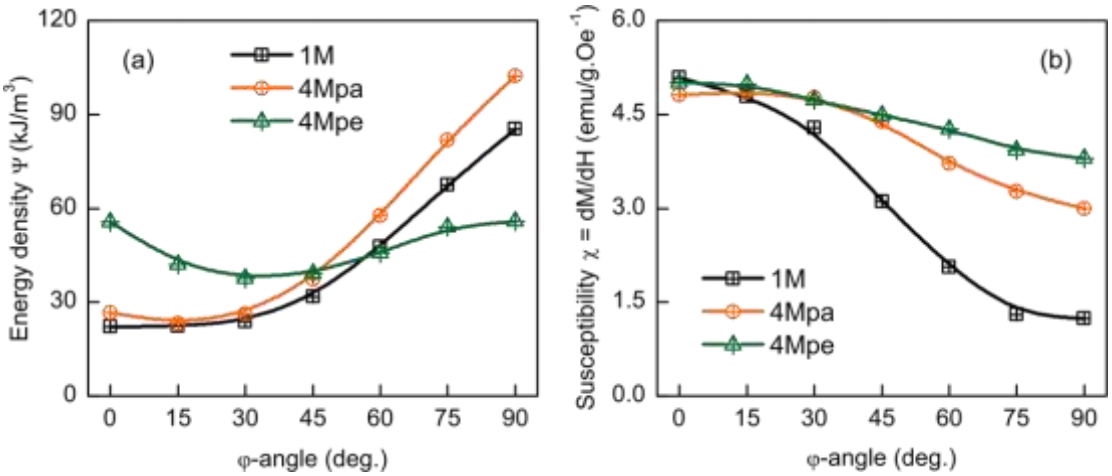

Figure 3. (a) The magnetic energy density Ψ and (b) the magnetic susceptibility by taking the area and the slope of M(H) loops depending on the orientation between the magnetic field and the based line.

The magnetic anisotropy energy density, denoted as $\psi = \mu_o \int_0^{M_s} HdM$, was quantitatively determined from the integrated area under the full magnetization hysteresis ($M(H)$) loops for each sample configuration. Fig. 3a displays the angular dependence of Ψ for the various sensor structures. For the 1M sample, Ψ exhibits a pronounced variation, increasing nearly fourfold from approximately 22 kJ/m^3 when the external field is aligned with the easy axis (EA, φ = 0°) to 85 kJ/m^3 when oriented perpendicular (φ = 90°). In the 4Mpa sample, this range is even broader, spanning from 26.6 to 102.4 kJ/m^3 (a 4.5-fold increase), whereas the 4Mpe sample demonstrates a more modest anisotropy, with Ψ varying from 33 to 64 kJ/m^3. These differences are attributed to the underlying magnetic anisotropy axes dictated by shape anisotropy, i.e., in the 1M and 4Mpa samples, the EA is predominantly aligned along the long bars, resulting in strong uniaxial anisotropy, while the 4Mpe structure, composed of orthogonally arranged segments, effectively averages the anisotropy axes, yielding a more isotropic response. Given that the fabrication process does not induce change in the structural properties of the developed sensor, which remains in its initial amorphous state, contributions from other forms of magnetic anisotropy are expected to be negligible. Consequently, the dominant source of magnetic anisotropy influencing the sensor's behavior in this study is attributed primarily to shape anisotropy. This is reflected in the $M(H)$ loops, where the 1M and 4Mpa samples display the most pronounced angular dependence of magnetization energy, particularly between φ = 30° and 75°, indicating strong anisotropy. As a direct consequence, the magnetic susceptibility $\chi = dM/dH$, extracted from the slope of the $M(H)$ loops and plotted in Fig. 3b, mirrors the anisotropy energy trends, i.e., the susceptibility is highly sensitive to φ in the 1M and 4Mpa samples, but remains relatively invariant in the 4Mpe configuration.

3.2. Numerical Magnetic Simulation

The architecture of each sample configuration consists of multiple interconnected bars of varying lengths, arranged in a continuous, perpendicular zigzag pattern. Owing to their distinct dimensions and orientations, each segment exhibits a unique response to external magnetic fields, resulting in a complex, spatially dependent magnetic behavior. The global magnetic characterization expressed through the $M(H)$ loop are insufficient to distinguish the individual contributions of magnetic field and anisotropy energy from the long (L-lines) and short (S-lines) bars, making it challenging to identify which regions predominantly govern the observed magnetic and MI effects. To elucidate the individual contributions, finite element method (FEM) simulations were performed using Ansys Maxwell software, employing the geometries of the actual fabricated prototypes and incorporating experimentally derived $B(H)$ hysteresis loops of the FeSiC ribbon as input parameters. In this study, the simulated geometries were discretized through FEM meshing utilizing the TAU algorithm to optimize mesh quality. To ensure high accuracy and reproducibility, the simulations were constrained to a maximum of 100,000 mesh elements, with a convergence criterion set at 1.0% relative error. External excitations, including the applied magnetic field and boundary conditions, were systematically incorporated into the simulation framework. At each mesh node, Maxwell's four differential equations governing electromagnetic fields were numerically solved. Subsequently, the spatial distributions of magnetic flux density, magnetization response, and magnetic field intensity within various regions of the simulated sensors under the applied magnetic field were computed and analyzed.

The simulated magnetization curves, presented in Fig. 4a, demonstrate good agreement with experimental data across different angles between the external field and the L-line axis, validating the reliability of the simulation approach. Figure 4b visualizes the spatial distribution of magnetic flux density within the meander structure under various field orientations, clearly revealing that the magnetic response is highly anisotropic and depends on the alignment of the external field relative to the Land S-line axes. Specifically, the L-lines exhibit dominant magnetization for field angles from 0° to 45° (Fig. 4, d1-d2), while the S-lines become increasingly magnetized as the field approaches 90°, where it aligns with their EAs (Fig. 4, d3). This anisotropic behavior, as elucidated by simulation, directly underpins the observed magnetic anisotropy in the single meander structures. Notably, the L-lines constitute approximately 84% of the total sample volume, and simulation analysis indicates that, for field angles below 60°, these segments contribute over 90% of the total magnetization; even at 90°, their contribution remains substantial at nearly 70%. Thus, despite the enhanced magnetization of the S-lines at high angles, the overall magnetic and MI properties of the meander structure are overwhelmingly governed by the L-lines.

Comprehensive finite element simulations using Ansys Maxwell were conducted on both the 4Mpa and 4Mpe configurations to elucidate the spatial distribution and anisotropy of magnetic flux under varying external field orientations. The results, depicted in Figure 5a, reveal pronounced anisotropic behavior in the 4Mpa sample, i. e., when the external magnetic field is aligned with the L-line axis (φ = 0°, Fig. 5, a1), the magnetic response is maximized, but it diminishes significantly as the field orientation shifts toward φ = 90° (Fig. 5, a3). This directional dependence is consistently observed across all individual meander elements within the structure. Quantitative analysis indicates that the difference in magnetic flux across this sample between these orthogonal measurement directions can approach 80% (Fig. 5c).

In contrast, the 4Mpe configuration exhibits a markedly different magnetic flux distribution. Except at φ = 45°, pairs of single meanders along the diagonal display equivalent flux patterns at other orientations, resulting in a substantial reduction in overall anisotropy. Consequently, the variation in magnetic flux and thus the MI response—between different measurement directions is reduced to approximately 20%. This simulation result is in coherent with experimental M (H) characterizations (Fig. 2), and can be attributed to the underlying anisotropy axis configuration, i.e., the 4Mpa sample possesses a dominant uniaxial EA along the L-line, whereas the 4Mpe sample features orthogonal, multi-axis EA distributions due to its perpendicular segment arrangement. These distinct anisotropic characteristics, dictated by meander configuration, are expected to yield highly anisotropic MI in the 4Mpa sample and more isotropic behavior in the 4Mpe sample.

3.3. Magnetoimpedance Characteristics

To quantitatively assess the MI effect in the fabricated sensors, the MI ratio, defined as the relative change in impedance under an external magnetic field, is employed as a key performance metric [15, 18]:

$$MI(\%) = \frac{Z(H) - Z(H=0)}{Z(H=0)} \times 100$$

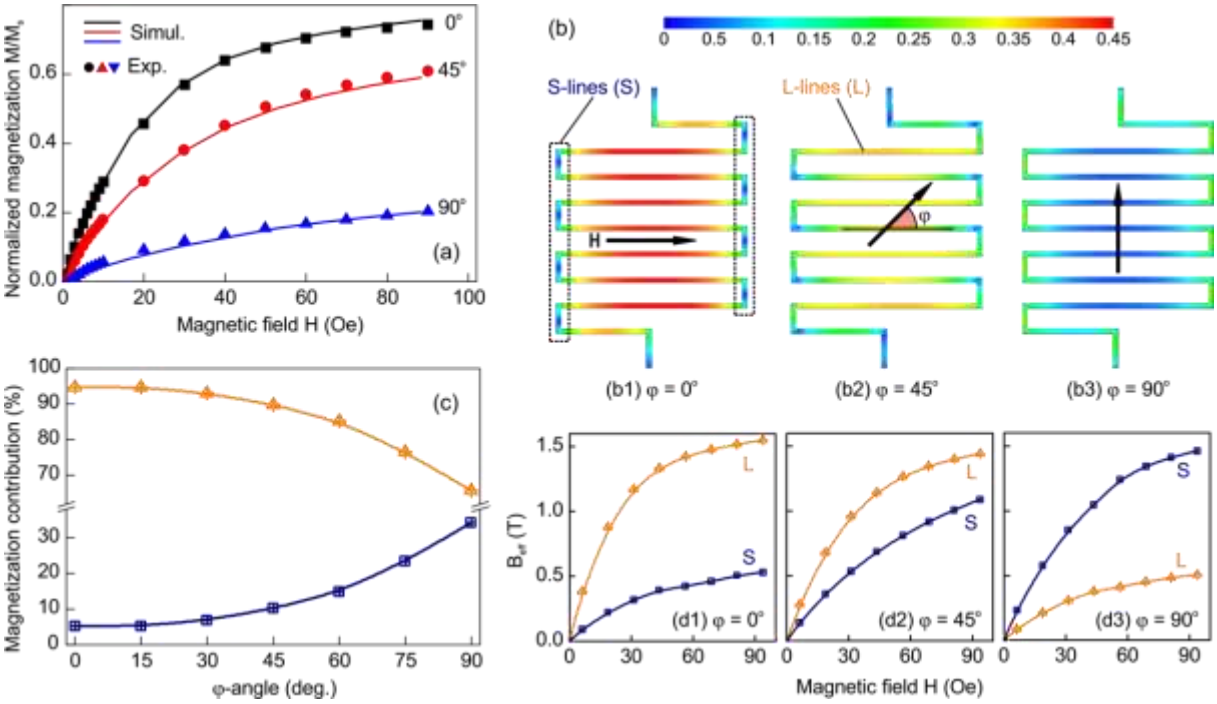

Figure 4. The simulation results: (a) Magnetic field dependence of magnetization, (b) magnetic flux density distribution in applied magnetic field of 10 Oe, (c) the φ-angle dependence of magnetization contribution and (d) the magnetic field dependence of magnetization analyzed for S-lines and L-lines with the different orientation angle φ varied from 0° to 90°.

Fig. 6 presents the frequency and magnetic field dependence of the impedance for various sensor configurations, including 1M, 4Mpa, and 4Mpe. Notably, the single meander sensor exhibits a broad resonance peak at a high frequency of 2.7 GHz. Upon increasing the number of meander elements to four (4Mpa and 4Mpe), the resonance peak becomes sharper and shifts toward lower frequencies, a trend more pronounced in the parallel configuration of 4Mpa than in the perpendicular configuration of 4Mpe (Fig. 6a). This frequency reduction is attributed to the increased inductance resulting from the combined meander elements, as described by the resonance condition [15, 18]. Specifically, the 4Mpa sample exhibits a resonant frequency of approximately 1.43 GHz, significantly lower than the 1.82 GHz observed for the 4Mpe sample, demonstrating that parallel meander integration is more effective in lowering the operational frequency range.

The MI ratio measured with the magnetic field aligned along the baseline (φ = 0°) for different sensor configurations is shown in Fig. 6d. All configurations display a rapid increase in the MI ratio at low magnetic fields, peaking near 50 Oe, followed by a gradual decline at higher fields. However, the magnitude of the MI ratio is highly dependent on sensor geometry. The 1M structure achieves a maximum MI ratio of approximately 18.6%. In contrast, the integration of four meander elements results in a substantial

enhancement, i.e., the 4Mpa sensor reaches a maximum MI ratio of 290%, while the 4Mpe configuration achieves 180%. These represent increases of 15.6-fold and 9.7-fold, respectively, compared to the 1M type. Thus, the parallel and perpendicular combination of meander units not only shifts the resonance to lower frequencies but also yields an order-of-magnitude improvement in MI ratio, illustrating the critical role of sensor architecture in optimizing MI performance for advanced sensing applications.

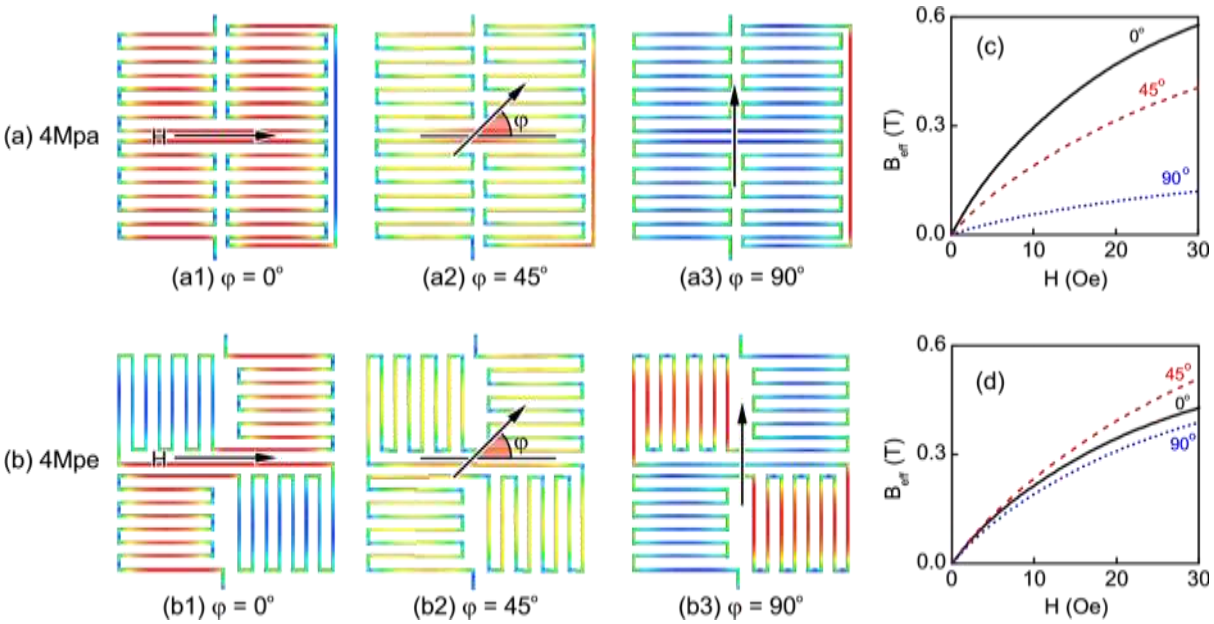

Figure 5. (a, b) The simulation results: Magnetic flux density distribution in applied magnetic field of 10 Oe and (c, d) low magnetic field dependence of magnetization analyzed for 4Mpa and 4 Mpe with the different orientation angle φ varied from 0° to 90°.

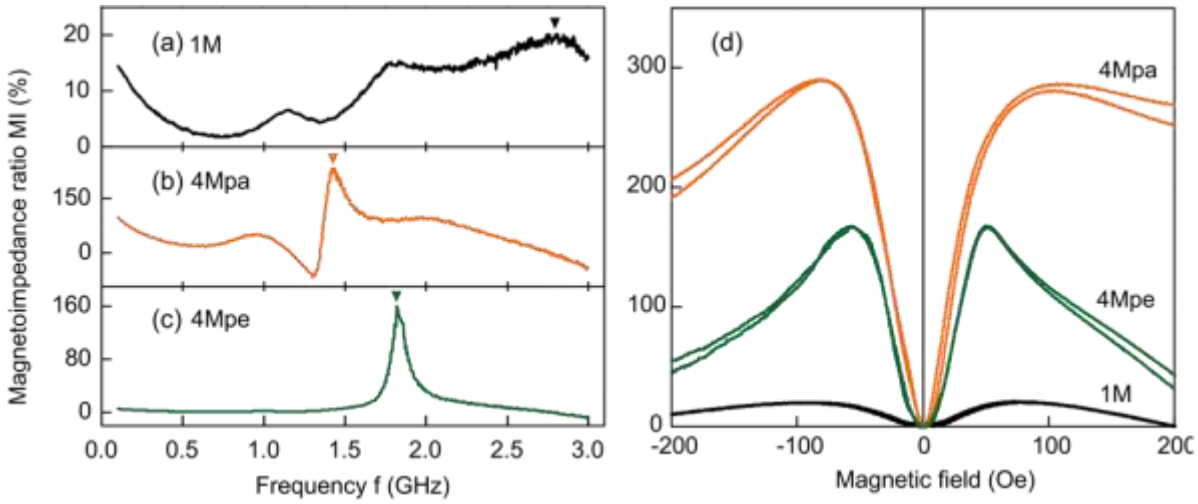

Figure 6. (a) Frequencies and (b) magnetic field dependence of magnetoimpedance MI ratio measured in various samples with different configuration from one to 4 meander units in parallel and perpendicular orientations.

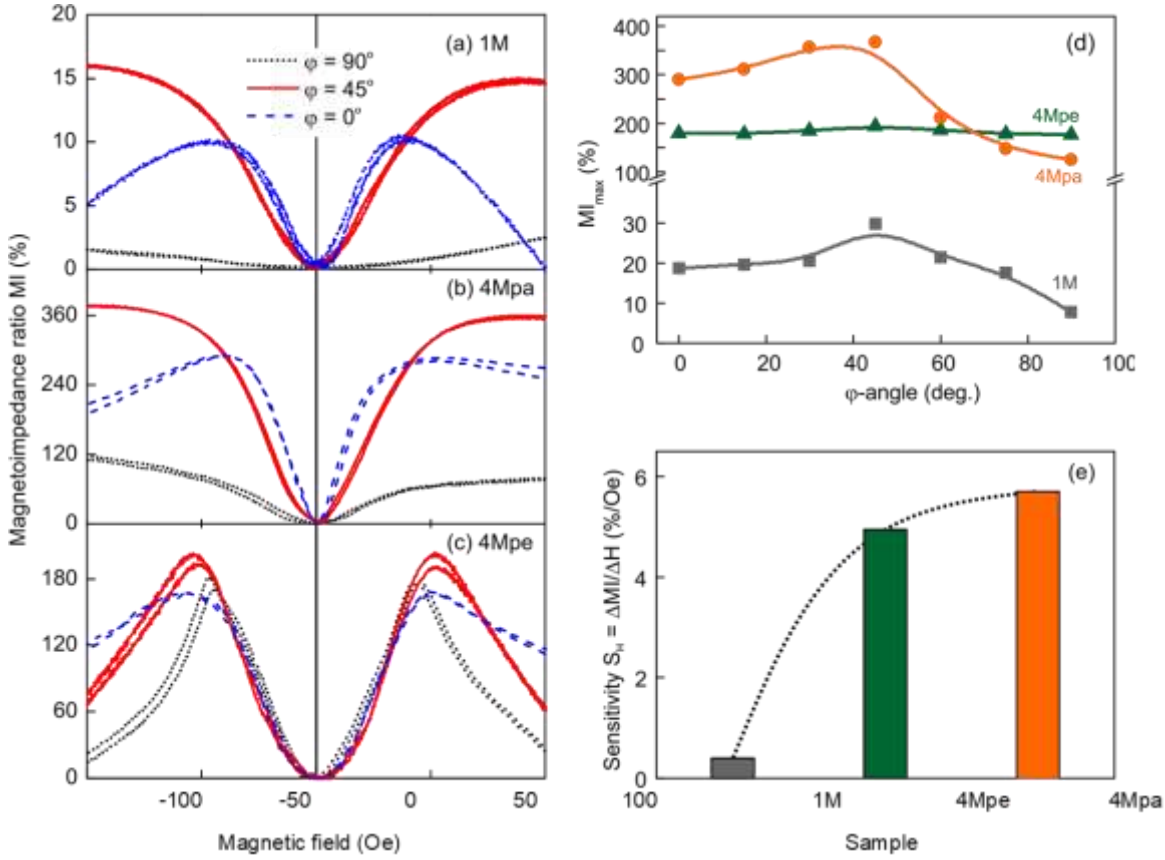

Figure 7. Magnetic field dependence of magnetoimpedance MI ratio measured at different magnetic field orientation with the based line in various samples with different configuration from one (a) to 4 meander units in parallel (b) and perpendicular arrangements (c); φ-angle dependence of maximum MI ratio (d) and MI sensitivity extracted from the MI curve slope (e) for different samples.

Fig. 7 (a-c) illustrates the MI response as a function of magnetic field orientation relative to the baseline for different sensor configurations. The 1M and 4Mpa samples exhibit a pronounced angular dependence in their MI curves, with the MI effect varying significantly as the φ changes. In contrast, the 4Mpe sample demonstrates minimal variation in MI response with respect to φ, indicating a near-isotropic behavior. Across all samples, the MI ratio undergoes its most substantial change at an intermediate angle of $\varphi = 45°$. Moreover, the slope of the MI curves, indicative of the sensor's response speed, is steepest at $\varphi = 0°$, reflecting maximum sensitivity when the magnetic field aligns with the baseline.

Fig. 7d quantifies the maximum MI ratio (MI_{max}) as a function of φ. The 1M sample exhibits a relatively low MI ratio below 30%, strongly dependent on angular orientation. The 4Mpa sample shows a similar angular trend but with a significantly enhanced MI ratio, reaching up to 400% at $\varphi = 45°$, representing a more than tenfold increase compared to the 1M sensor. Conversely, the 4Mpe sample maintains an almost constant MI ratio across all angles, exhibiting its isotropic magnetic response. Magnetic field sensitivity ($SH = \Delta MI/\Delta H$), derived from the steepest MI slopes and plotted in Fig. 7e, further confirms these findings, i.e., the 1M sensor exhibits the lowest sensitivity (0.5 %/Oe), whereas both 4Mpa and 4Mpe configurations achieve comparable, substantially higher sensitivities of approximately 5.7 %/Oe and 5%/Oe, respectively.

These results highlight the trade-offs inherent in sensor design such as: i) The 4Mpa configuration markedly amplify the MI effect but induce strong angular dependence, making them ideal for applications

requiring directional sensitivity, and in contrast; and ii) The 4Mpe configuration provide enhanced MI ratios with minimal angular variation, suitable for isotropic magnetic field detection. Notably, the 4Mpe sensors operate effectively over a broad magnetic field range from -50 to 50 Oe regardless of field orientation and exhibit advantageous low-frequency operation conducive to electronic integration. Thus, the choice between 4Mpa, and 4MPe combinations should be application-driven, balancing sensitivity, angular dependence, and operational frequency.

The experimental impedance and MI characteristics align well with theoretical analyses and finite element simulations, which attribute the anisotropic behavior in 1M and 4Mpa samples to uniaxial easy axis alignment along the L-lines, while the 4Mpe sample's isotropy arises from orthogonal multi-axis anisotropy. This comprehensive understanding facilitates the rational design of MI sensors with tailored directional sensitivities for diverse technological applications. Furthermore, the developed MI sensors have emerged as highly promising candidates for high-sensitivity magnetic field detection, attributable to their unique geometric configurations and favorable impedance responses under external magnetic stimuli. A critical factor influencing their practical implementation is the longterm stability of the MI effect, which is predominantly governed by the intrinsic quality of the magnetic thin films and their resilience to environmental variables such as humidity and temperature fluctuations. Recent investigations have demonstrated that employing soft magnetic materials with stable magnetic anisotropy, specifically Fe-based amorphous alloys, substantially enhances both thermal and magnetic stability, thereby ensuring a consistent impedance response throughout prolonged operational durations [19, 20].

Durability represents another pivotal parameter, particularly in applications exposed to mechanical vibrations or cyclic thermal stresses. MI sensors fabricated on rigid substrates utilizing laser engraving combined with wet chemical etching techniques have exhibited robust mechanical integrity. Additionally, the application of protective coatings and encapsulation strategies has the potential to further augment resistance against corrosion and physical degradation, thereby extending sensor longevity under harsh environmental conditions without significant deterioration in performance. Regarding applicability, MI sensors demonstrate high sensitivity at ambient temperature and exhibit compatibility with miniaturized electronic platforms, rendering them suitable for diverse applications. These include non-contact current sensing, structural health monitoring, and biomedical diagnostics, underscoring their versatility and potential for integration into advanced sensing systems.

4. Conclusion

The obtained results in this work demonstrate the fabrication of MI sensors with distinct configurations on miniaturized iron-based soft magnetic ribbon using laser engraving and chemical etching. The VSM confirms the soft magnetic nature of the sensor material. Angular dependent magnetic measurements reveal that anisotropy can be actively controlled by selecting uniaxial 4Mpa or biaxial 4Mpe configurations. The multi-meander combinations significantly enhance the MI effect by approximately one order of magnitude compared to conventional 1M sensors, while enabling tunable isotropic or anisotropic magnetic field responses. Experimental observations are substantiated by finite element simulations elucidating the role of transverse magnetization dynamics. This multi-meander design offers versatile pathways for developing MI sensors with tailored sensitivity to magnetic field magnitude and direction, promising broad applicability in biomedical, industrial, and defense sectors.

Acknowledgements

This work was supported by the National Research Program under the granted Research Project No. ĐTĐL.CN-02/23.

References

[1] Sayad, E. Skafidas, P. Kwan, Magneto-Impedance Biosensor Sensitivity: Effect and Enhancement, Sensors, Vol. 20, No. 18, 2020, pp. 5213.

[2] K. Mohri, M. Yamamoto, T. Uchiyama, Application Topics of Amorphous Wire Cmos Ic Magneto-Impedance Micromagnetic Sensors for I-O-T Smart Society, Journal of Sensors, Vol. 2019, No. 1, 2019, pp. 8285240.

[3] J. M. Coey, Magnetism And Magnetic Materials, Cambridge University Press, 2010.

[4] J. Nabias, A. Asfour, J. P. Yonnet, Use of Magnetic Circuits for Toroidal Gmi Current Sensors, IEEE Sensors Journal, Vol. 19, No. 13, 2019, pp. 4866-4873.

[5] P. Ripka, M. Janosek, Advances in Magnetic Field Sensors, IEEE Sensors Journal, Vol. 10, No. 6, 2010, pp. 1108-1116.

[6] M. H. Phan, H. X. Peng, Giant Magnetoimpedance Materials: Fundamentals and Applications, Progress in Materials Science, Vol. 53, No. 2, 2008, pp. 323-420.

[7] L. Panina, K. Mohri, Magneto-Impedance Effect in Amorphous Wires, Applied Physics Letters, Vol. 65, No. 9, 1994, pp. 1189-1191.

[8] C. Kittel, Theory of the Dispersion of Magnetic Permeability in Ferromagnetic Materials at Microwave Frequencies, Physical Review, Vol. 70, No. 5-6, 1946, pp. 281.

[9] H. Kikuchi, S. Oe, H. Uetake, S. Yabukami, T. Nakai, S. Hashi, K. Ishiyama, Enhancement of Sensitivity on Miniaturized Thin-Film Magnetoimpedance With Ellipsoidal Element, Physics Procedia, Vol. 75, 2015, pp. 1271-1278.

[10] A. G. Arribas, E. F. Andez, A. V. Svalov, G. V. Kurlyandskaya, A. Barrainkua, D. Navas, J. M. Barandiaran, Tailoring the Magnetic Anisotropy of Thin Film Permalloy Microstrips by Combined Shape and Induced Anisotropies, the European Physical Journal B, Vol. 86, 2013, pp. 1-7.

[11] L. Chen, Y. Zhou, C. Lei, Z. M. Zhou, W. Ding, Effect of Meander Structure and Line Width on Gmi Effect in Micro-Patterned Co-Based Ribbon, Journal of Physics D: Applied Physics, Vol. 42, No. 14, 2009, pp. 145005.

[12] L. Chen, Y. Zhou, C. Lei, Z. Zhou, W. Ding, Giant Magnetoimpedance Effect in Sputtered Single Layered Nife Film and Meander Nife/Cu/Nife Film, Journal of Magnetism and Magnetic Materials, Vol. 322, No. 19, 2010, pp. 2834-2839.

[13] V. Zhukova, J. Blanco, M. Ipatov, M. Churyukanova, J. Olivera, S. Taskaev, A. Zhukov, Optimization of High Frequency Magnetoimpedance Effect of Fe-Rich Microwires By Stress-Annealing, Intermetallics, Vol. 94, 2018, pp. 92-98.

[14] D. Garcia, V. Raposo, O. Montero, J. Iniguez, Influence of Magnetostriction Constant on Magnetoimpedance–Frequency Dependence, Sensors and Actuators A: Physical, Vol. 129, No. 1-2, 2006, pp. 227-230.

[15] V. M. Garc´Ia-Chocano, H. Garc´Ia-Miquel, Dc And Ac Linear Magnetic Field Sensor Based on Glass Coated Amorphous Microwires with Giant Magnetoimpedance, Journal of Magnetism and Magnetic Materials, Vol. 378, 2015, pp. 485-492.

[16] H. A. Tam, N. V. Tuan, N. T. Ngoc, L. V. Lich, D. V. Hai, M. H. Phan, C. G. Kim, V. D. Lam, D. T. H. Giang, Tuning Rotational Magnetization for High Frequency Magnetoimpedance in Micro-Patterned Triangle Spiral Magnetic Systems, Journal of Science: Advanced Materials and Devices, Vol. 7, No. 4, 2022, pp. 100514.

[17] V. N. Thuc, H. A. Tam, N. H. Duc, N. T. Ngoc, V. T. N. Khanh, L. V. Lich, V. H. Dinh et al., Hierarchical Geometric Designs for Fe-Based Amorphous Materials with Tunable Soft Magnetic Properties, Journal of Alloys and Compounds, Vol. 895, 2022, pp. 162628.

[18] A. Asfour, J. P. Yonnet, M. Zidi, A High Dynamic Range Gmi Current Sensor, 2012.

[19] Y. Song, M. Jia, M. Lin, X. Li, W. Lu, Thermal Stability, Magnetic Properties and Gmi Effect of Cr-Doping Amorphous Cofesib Ribbons, Journal of Alloys and Compounds, Vol. 622, 2015, pp. 500-503.

[20] L. Pan, L. Ma, H. Wu, X. Li, Y. Ye, J. Wang, Q. Liu, Optimization of Temperature Stability and Sensitivity of the Giant Magnetoimpedance Effect in Meander Shaped Co-Based Amorphous Ribbon Using Dc-Biased Current for Sensor Application, Journal of Physics D: Applied Physics, Vol. 56, No. 34, 2023, pp. 345001.